



# Selective laser melting of thermal pre-treated metal oxide doped aluminum oxide granules



Stefan Pfeiffer<sup>a,b,\*</sup>, Malgorzata Makowska<sup>c</sup>, Kevin Florio<sup>d</sup>, Dario Ferreira Sanchez<sup>c</sup>, Federica Marone<sup>c</sup>, Xiaoyan Zhang<sup>a</sup>, Christos G. Aneziris<sup>b</sup>, Helena Van Swygenhoven<sup>c</sup>, Konrad Wegener<sup>d</sup>, Thomas Graule<sup>a,b</sup>

<sup>a</sup> Laboratory for High Performance Ceramics, Empa – Swiss Federal Laboratories for Materials Science and Technology, Überlandstrasse 129, 8600, Dübendorf, Switzerland

<sup>b</sup> Institute of Ceramic, Glass and Construction Materials, TU Bergakademie Freiberg, Agricolastraße 17, 09599, Freiberg, Germany

<sup>c</sup> Photon Science Division, Paul Scherrer Institut, 5232, Villigen PSI, Switzerland

<sup>d</sup> Institute of Machine Tools and Manufacturing, ETH Zürich, Leonhardstrasse 21, 8092, Zurich, Switzerland

## ARTICLE INFO

### Keywords:

Selective laser melting of alumina  
Powder density  
Tomographic microscopy

## ABSTRACT

The influence of powder bed density on the final density and microstructure of aluminum oxide parts manufactured by direct selective laser melting has been studied. Iron oxide and manganese oxide nanoparticles were used to improve laser absorption by over eighty percent. To achieve such values, flowable doped alumina granules were prepared by spray drying. Thermal treatment of the granules at 1600 °C and consecutive mixing with coarse alumina allowed improvement of the tapped powder densities, reaching a maximum value of 56.4% of the theoretical density. This led to laser processed parts with densities up to 98.6% measured by tomographic microscopy. Measurements with an integrating sphere and an UV-VIS-NIR spectrophotometer employing Kubelka-Munk theory show the decrease of absorptance caused by thermal pre-treatment. 3D mapping by X-ray  $\mu$ -beam fluorescence contrast tomography and high resolution synchrotron powder diffraction provide information about the variation of dopant distribution and composition within the granules.

## 1. Introduction

Selective laser melting and sintering (SLM and SLS) are well established in industry for shaping of parts with complex geometries. However, its industrial usage is limited to applications employing metals or polymers, since these materials undergo plastic deformation and are therefore less critical to cracking due to thermal stresses. Nevertheless, SLM and SLS have a great potential to produce highly complex ceramic prototypes and small series with high accuracy and short lead times and to avoid cost, energy and time consuming machining.

In the past, several approaches to overcome the problems of low thermal shock resistance and weak densification during processing of oxide ceramics were demonstrated. For example, the use of different lasers (CO<sub>2</sub> [1–4], pulsed Nd-YAG [5,6], high power diode [7] or femtosecond lasers [8]), various laser scanning strategies (special circular [9], single-track, zigzag or island scanning strategies using different laser powers [10] or powder feeding directly to the melt pool [11,12]),

preheating (by microwaves [13], a second laser [14,15] or a building platform with a vertical tube furnace [4]) and finally the addition of silica to form an amorphous phase [1,2,5,6] were tested to improve the properties of the laser processed parts. Until now, none of these approaches proved to combine a high accuracy, a high bending strength and a total freedom of design. To achieve this, not only the laser process parameters and processing conditions have to be considered, but also powder properties, such as melting temperature, absorptance [16] flowability and powder bed density [17,18]. It is stated that high powder bed densities are necessary to achieve a high density of the final parts [17,18] and that strength of ceramic parts decrease with increasing porosity [19]. Since traditionally only fine-grained ceramic parts show adequate mechanical properties at room temperature, particles with sizes in the range of tens of nanometers to a few micrometers are preferred. However, agglomeration of particles with a diameter below 10  $\mu$ m must be considered [20], which will decrease the powder bed density, homogeneity and flowability [17]. Dense powder beds consisting of fine

\* Corresponding author. Laboratory for High Performance Ceramics, Empa – Swiss Federal Laboratories for Materials Science and Technology, Überlandstrasse 129, 8600, Dübendorf, Switzerland.

E-mail address: [stefan.pfeiffer@empa.ch](mailto:stefan.pfeiffer@empa.ch) (S. Pfeiffer).

<https://doi.org/10.1016/j.oceram.2020.100007>

Received 27 April 2020; Received in revised form 5 June 2020; Accepted 10 June 2020

Available online 12 June 2020

2666-5395/© 2020 The Author(s). Published by Elsevier Ltd on behalf of European Ceramic Society. This is an open access article under the CC BY license (<http://creativecommons.org/licenses/by/4.0/>).

**Table 1**

Absolute densities, specific surface area and BET average particle size of raw powders.

Raw material	Al <sub>2</sub> O <sub>3</sub> AA18	Al <sub>2</sub> O <sub>3</sub> AA3	Al <sub>2</sub> O <sub>3</sub> Taimicron TM-DAR	Fe <sub>2</sub> O <sub>3</sub> L2715D	MnO <sub>2</sub> US3319
Absolute density [g/cm <sup>3</sup> ]	3.99	4.01	3.95	4.38	4.28
Specific surface area [m <sup>2</sup> /g]	<0.1	0.4	11.8	69.7	22.7
BET average particle size [nm]		3700	128.8	19.6	61.7

particles could be already deposited by an aerosol assisted spraying technique [3], by electrophoretic deposition [4] or by slurry casting on a substrate, where water was evaporated before the laser treatment [1,2]. Spray granulation provides an alternative solution for this problem. It offers the possibility of homogeneous particle distribution and optimized layer thickness for fast processing with high accuracy. It was already applied by Juste et al. [21] and Mapar et al. [22,23], who obtained highly flowable granules ensuring a dense powder bed.

Alumina shows low absorption in the visible or near infrared range (3% absorption at 1064 nm [24]). To improve the interaction between a fiber laser and alumina powder, carbon [21,25–28] and SiC [27] were mixed together with alumina particles by mechanical blending and tested as suitable absorbers in the near infrared region. In this work, alumina granules are directly doped with Fe<sub>2</sub>O<sub>3</sub> and MnO<sub>2</sub>/Mn<sub>2</sub>O<sub>3</sub> nanoparticles during spray drying, since these dopants are known as effective absorbers to improve the absorption of alumina granules in the visible and near infrared range [16,29–32]. These dopants can have a significant influence on microstructure, phase composition and properties of sintered alumina, which has already been extensively studied in the past for conventional sintered alumina. For example, a complex series of oxides can arise by thermal treatment in manganese-doped alumina, since manganese shows a variable valency change. Thus, different manganese cations with different valency states can replace the aluminum cations in the lattice, which results in fast diffusion lowering the energy required for sintering [33,34]. It is already established that up to 2% manganese oxide increases grain growth in Al<sub>2</sub>O<sub>3</sub> and promotes excessive irregular grain growth [35]. A density between 98 and 99% [33,36] was reached for sintering temperatures between 1550 °C and 1650 °C independent of the amount of the dopant. Aluminum oxide doped with manganese showed increased hardness and flexural strength [33,36]. Fe<sub>2</sub>O<sub>3</sub> also enhances sintering [33] by entering the lattice of alumina [34]. Preliminary studies on iron oxide doped alumina granules showed that thermal treatment in air leads to this homogeneous incorporation. At 1600 °C a single corundum type phase was created, where iron diffused in the alumina lattice [37]. With more than 1% of iron oxide the grain growth is inhibited and results in equiaxed, spheroidal grains [35]. Ferric oxide doped alumina samples showed an almost consistent flexural strength up to 0.1 wt%, a slight decrease up to 2 wt% and a following strong decrease as the ferric oxide amount was further increased [38]. By seeding the alumina with 4 wt% iron oxide the temperature to reach full density could be lowered to 1350 °C [39].

In this work the influence of different dopants and thermal pretreatment temperatures on powder bed density, flowability, absorption and phase composition of spray dried alumina granules is evaluated, as well as the influence on laser processing, especially on density and microstructure. To achieve high packing densities in the powder beds, spray dried granules were made from bimodal distributions of alumina powders within the granules according to McGeary [40] and Pfeiffer et al. [31], thermally treated in air up to 1600 °C and mixed with coarser alumina to maintain a high flowability. The homogeneous addition of

manganese oxide or iron oxide to the aluminum oxide granules increased the powder bed absorptance. With these steps, the necessary dopant amount could be reduced and CO<sub>2</sub> formation could be avoided. Aluminum oxide parts with densities up to 98.6% were successfully manufacture using a frequency doubled pulsed green Nd-YAG laser ( $\lambda = 532$  nm) laser, which in theory provides a high resolution and the possibility to manufacture parts with relatively low stresses, since it offers a nominal average output power of only 5.75 W. Even with a low dopant amount of less than 1 vol% in the final powder, a formation of spinel phases was observed for both dopants after the laser treatment, which was not expected from traditionally evaluated phase diagrams.

## 2. Experimental

### 2.1. Starting materials

To achieve bimodal distributions of alumina within the spray dried granules, submicron  $\alpha$ -alumina Taimicron TM-DAR (Taimei Chemicals Co. LTD, Japan) and spherical micron-sized  $\alpha$ -alumina AA3 (Sumitomo, Chemical Co. LTD, Japan) were used. Additionally, spherical nano- $\alpha/\gamma$ -Fe<sub>2</sub>O<sub>3</sub> (L2715D, BASF SE, Germany) and nano-MnO<sub>2</sub> particles (US3319, US Research Nanomaterials, USA) were introduced during spray drying to improve the absorption of the green laser light. Coarse alumina AA18 (Sumitomo, Chemical Co. LTD, Japan) was added to the spray dried granules to increase the density of the powder bed after thermal treatment. The use of ammonium citrate dibasic p.a. 98% (Sigma Aldrich Corp., USA) as surfactant and PEG 35000 (Sigma Aldrich Corp., USA) as binder guaranteed a homogeneous dispersion of all particles in water as well as non-broken granules with high strength. For pH-value adjustment of the MnO<sub>2</sub> dispersion a 10% diluted ammonium hydroxide solution (Carl Roth GmbH + Co. KG, Germany) was utilized.

The absolute densities of all powders were measured by helium pycnometry (AccuPyc II 1340, Micromeritics, USA). BET (Brunauer–Emmett–Teller) measurements (SA 3100 Surface Area Analyzer, Beckman Coulter, Germany) provided the specific surface area (SSA) of the particles. Prior to the measurements, the raw powders were degassed with synthetic air for 2 h at 180 °C to remove adsorbed water from the surfaces (SA-PREP Surface Area Outgasser, Beckman Coulter, Germany). For all these powders a BET average particle size was calculated from the absolute density and the corresponding SSA assuming monomodal spherical particles according to the Sauter mean diameter [41]. The surface area of AA18 was too small to evaluate an accurate value for the SSA. To determine the surface potential and the saturation amount of the dispersant on the particle surfaces, zeta potential measurements were carried out by an electroacoustic method with a ZetaProbe Analyzer (Colloidal Dynamics, USA). The saturation amount of the dispersant, which should guarantee high surface potential of the particles for homogeneous dispersion in Nanopure water and low residuals of dispersant in the spray dried granules, was found by evaluation of the change of PZC (point of zero charge) as a function of added amount. Zeta potential measurements were conducted with an equilibration delay of 30 s. To adjust the pH of the utilized 5 wt% suspensions a 0.1 M solution of HCl (Carl Roth GmbH + Co. KG, Germany) and 0.1 M NaOH (Sigma Aldrich Corp., USA) were added. Required dielectric constants were taken from literature [42]. Particle size distributions of the dispersed starting materials were measured in water by laser diffraction (LS 13320, Beckman Coulter GmbH, Germany) and dynamic light scattering (ZetaSizer Nano ZS, Malvern Panalytical Ltd, United Kingdom). The required refractive indexes and extinction coefficients for both size measurements were taken from Ref. [43] for Fe<sub>2</sub>O<sub>3</sub>, Al<sub>2</sub>O<sub>3</sub> and from Ref. [44] for MnO<sub>2</sub>.

### 2.2. Spray granulation, thermal treatment and mixing with coarse alumina

Spray granulation was performed in the Mini spray dryer B-290 (Büchi Labortechnik AG, Switzerland) with an ultrasonic atomizer in co-current mode. For the granulation of a bimodal distribution of alumina, 72.6% of micron-sized AA3 and 27.4% of Taimicron TM-DAR was chosen [31,40].

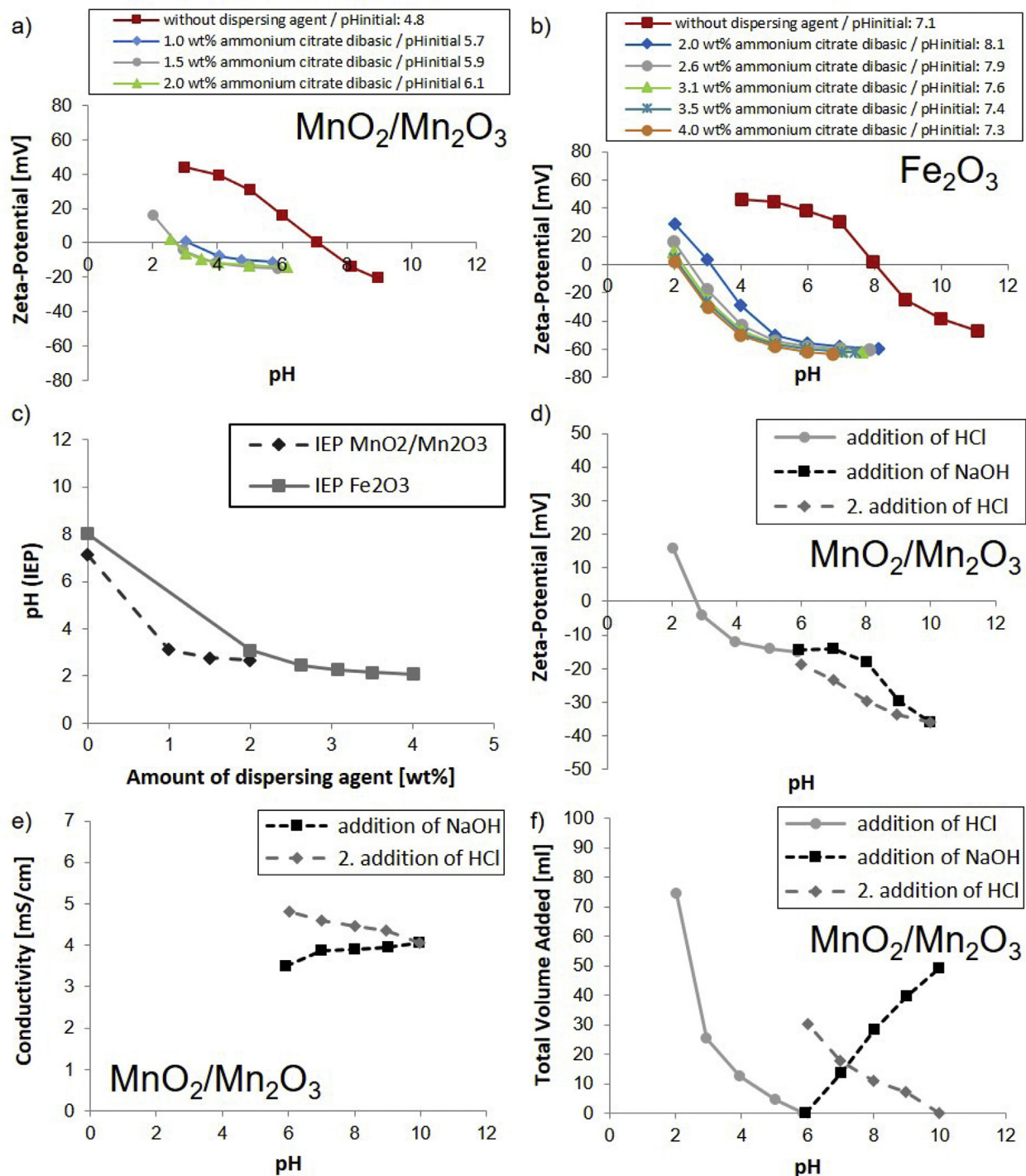


**Fig. 1.** Zeta potential of a)  $\text{MnO}_2/\text{Mn}_2\text{O}_3$  and b)  $\text{Fe}_2\text{O}_3$  [31] nanoparticles as a function of pH value and various citrate concentrations. c)  $\text{pH}_{\text{IEP}}$  of  $\text{MnO}_2/\text{Mn}_2\text{O}_3$  and  $\text{Fe}_2\text{O}_3$  [31] suspensions as function of ammonium citrate dibasic addition. d) Zeta potential of  $\text{MnO}_2/\text{Mn}_2\text{O}_3$  with 1.5 wt% (4.0 vol%) ammonium citrate dibasic as function of pH value and e) corresponding conductivity change by HCl and NaOH addition as function of pH value and f) added volume.

The total solid load in the slurry for spray drying was 50 vol%. Before spray drying, both alumina powders were separately mixed with  $\text{ZrO}_2$  milling balls (1 mm diameter for Taimicron TM-DAR or 5 mm diameter for AA3), dispersing agent and Nanopure water and afterwards dispersed by roll milling in polyethylene bottles for 20 h. The dopants were dispersed in water with 0.4 mm milling balls using a combination of vibration milling for 20 min with a vibrational frequency of 30 Hz (Retsch MM301, Retsch GmbH, Germany) and an additional roll milling step for 20 h. The binder PEG 35000 (2 wt% (6.1 vol%) of total powder amount) was added to AA3

after rotating for 1 h on the rolling bench. To obtain the final slurry for spray granulation, the individual dispersions were mixed and additionally homogenized for 4 h on a rolling bench. After removing the milling balls, the slurry was continuously stirred to prevent demixing. Process parameters for spray drying were an inlet temperature of 140 °C, an outlet temperature of 90 °C, an air flow rate within the spraying apparatus of 25 m<sup>3</sup>/h, an ultrasonic nozzle power of around 10 W, a nozzle frequency of 60 kHz and a slurry feed rate of a peristaltic pump of circa 2 ml/min. The Dehumidifier B-296 (B üchi Labortechnik AG, Switzerland) supplied constant and

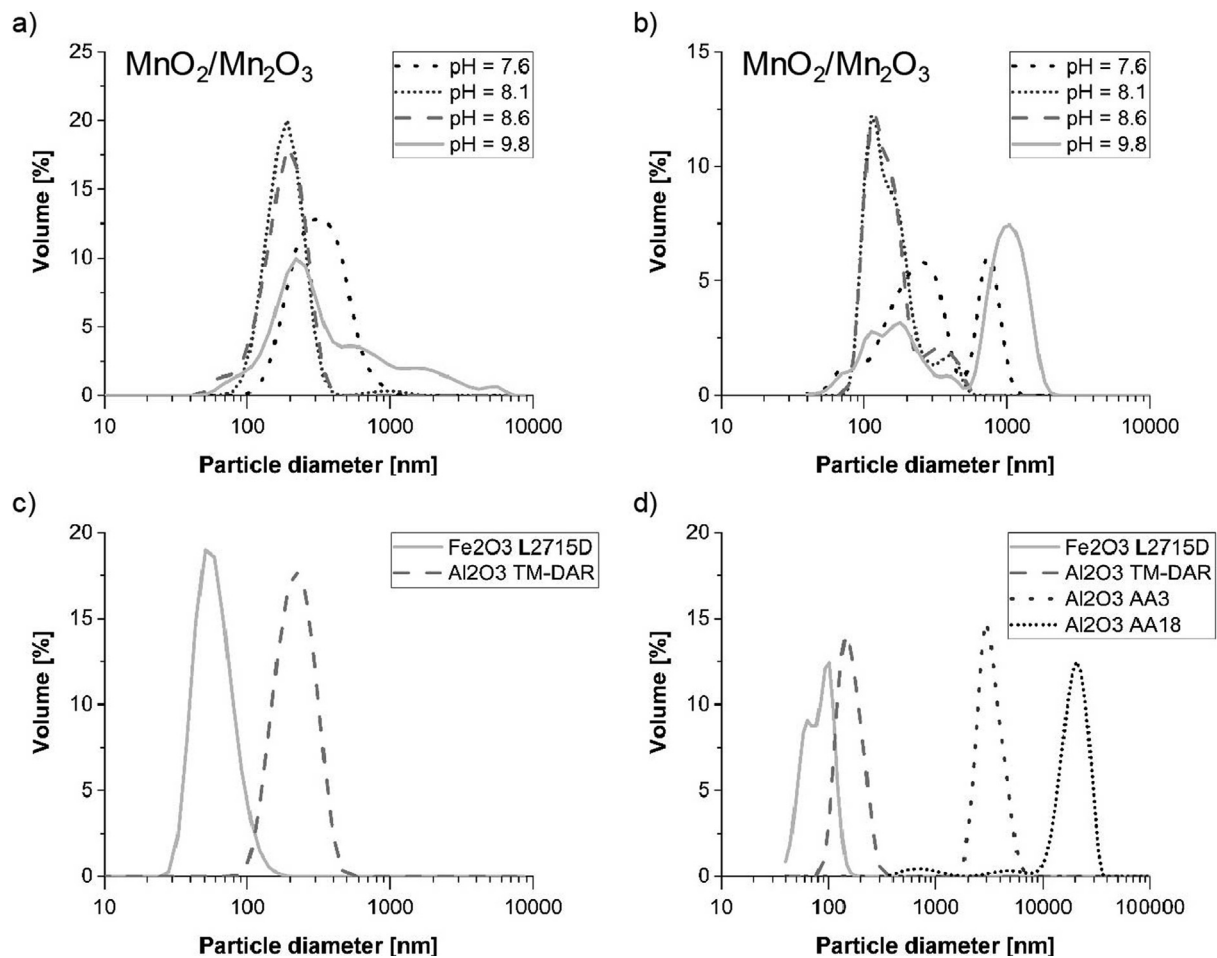


**Fig. 2.** a) Volume-based differential DLS particle size distribution of  $\text{MnO}_2/\text{Mn}_2\text{O}_3$  and b) volume-based differential LD particle size distribution of  $\text{MnO}_2/\text{Mn}_2\text{O}_3$  in water dispersed by means of ammonium citrate at different pH values. c) Volume-based differential DLS particle size distribution and d) volume-based differential LD particle size distribution of other powders in water dispersed by means of ammonium citrate.

**Table 2**

$d_{10}$ ,  $d_{50}$  and  $d_{90}$  of volume based particle size distributions of dispersed powders in water determined by dynamic light scattering (DLS) and Laser diffraction (LD).

Powder	$\text{Al}_2\text{O}_3$ AA18		$\text{Al}_2\text{O}_3$ AA3		$\text{Al}_2\text{O}_3$ Taimicron TM-DAR		$\text{Fe}_2\text{O}_3$ L2715D		$\text{MnO}_2$ US3319			
									pH = 8.1		pH = 8.6	
Measurement method	LD	LD	LD	DLS	LD	DLS	LD	DLS	LD	DLS	LD	DLS
$d_{10}$	10.9 $\mu\text{m}$	2.2 $\mu\text{m}$	109 nm	133 nm	51 nm	37 nm	95 nm	116 nm	95 nm	102 nm		
$d_{50}$	18.6 $\mu\text{m}$	3.0 $\mu\text{m}$	148 nm	201 nm	79 nm	53 nm	134 nm	172 nm	133 nm	172 nm		
$d_{90}$	26.1 $\mu\text{m}$	4.4 $\mu\text{m}$	212 nm	295 nm	110 nm	82 nm	257 nm	248 nm	287 nm	250 nm		

reproducible humidity conditions. The final granule separation was accomplished in a cyclonic collector and an additional screening step with a 120 mesh (125  $\mu\text{m}$ ) sieve (Retsch GmbH, Germany), since only a fine fraction was suitable to achieve good resolution and to connect properly the different layers during laser processing.

Thermal treatment of the spray dried granules was carried out in air in a high temperature furnace (LHT 04/17, Nabertherm GmbH, Germany). The applied temperature varied from 1400 up to 1600  $^{\circ}\text{C}$ . Holding times of 2 and 4 h were used with a heating rate of 2  $^{\circ}\text{C}/\text{min}$ . After thermal treatment the powders were screened with a 120 mesh sieve and finally mixed with 30 vol% coarse alumina AA18 on a rolling bench for 1 h according to Ref. [31].

### 2.3. Granule characterization

#### 2.3.1. Apparent and tapped density, flowability and particle size distribution

The quality of the as-prepared and thermal treated granules with and

without AA18 was characterized by several techniques. Apparent density was measured with a setup (PTL Dr. Grabehorst GmbH, Germany) according to the standard DIN EN ISO 23145-2. A jolting volumeter (JEL STAVII, J. Engelsmann AG, Germany) was used to determine the tapped density by tapping the sample 1000 times with a displacement of 3 mm in compliance to EN ISO 787-11. Relative densities were calculated as fractions of the apparent and tapped density over the absolute powder density. The ratio of tapped density divided by apparent density (Hausner ratio) was used to grade the flowability of the powders. The Hausner ratio is a commonly used parameter in the field of selective laser melting of different metals [45–48] and ceramics such as alumina and zirconia [25,27] and relates to frictional conditions in a moving powder [46,48]. It gives a quantitative prediction of the powder deposition behavior by an easy measurement method [49]. In general, a Hausner ratio below 1.25 is considered as an indicator for a suitable flowability of powders for selective laser melting [25,47]. Powder with a higher Hausner ratio and thus a poor flow behavior can result in localized porosity [48]. Moisture



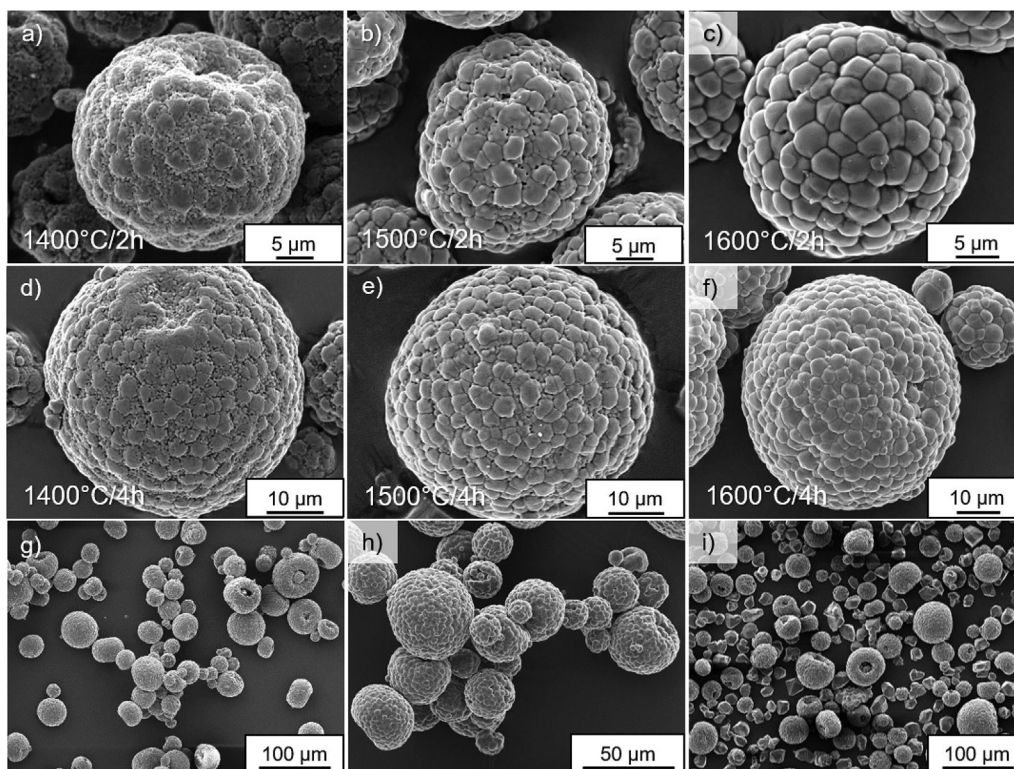


**Fig. 3.** SEM images of spray dried granules thermally treated at a) maximum temperature: 1400 °C/holding time: 2 h, b) 1500 °C/2 h, c) 1600 °C/2 h, d) 1400 °C/4 h, e) 1500 °C/4 h, f) 1600 °C/4 h. Illustration by SEM of g), h) sintering necks between the granules and formed agglomerates after thermal treatment at 1600 °C and i) de-agglomeration by mixing with AA18.

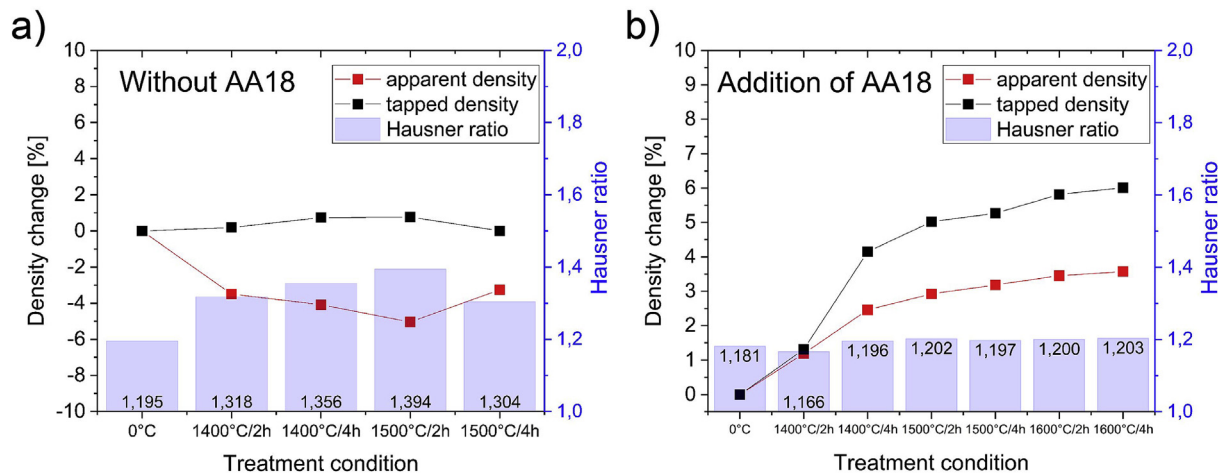


**Fig. 4.** Apparent and tapped density change as well as Hausner ratio of thermal treated granules in respect to treatment conditions (temperature/holding time) a) without addition of AA18 and b) with addition of AA18.

content of the different powders was measured at 140 °C for 1 h with the moisture analyzer HR83 (Mettler Toledo GmbH, Switzerland). The fraction of the received fine granules after spray drying and sieving to the weight of all solid contents in the slurry before spray drying revealed the total yield of granules suitable for laser processing. The characteristic values for  $d_{10}$ ,  $d_{50}$  and  $d_{90}$  were measured by laser diffraction (LS 13320, Beckman Coulter GmbH, Germany) in isopropanol.

### 2.3.2. Electron microscopy

The influence of different temperatures and holding times on the microstructure of the doped granules was visualized and studied by Scanning Electron Microscopy (VEGA3 Tescan, Tescan instruments,

Czech Republic). Prior to the SEM studies, the powder was attached to an adhesive carbon tab and distributed with compressed air. Sputtering with Au-Pd (Sputter coater 108 auto, Tescan instruments, Czech Republic) was performed twice using angles of 45° and 90° (sample carrier to sputter direction). For imaging of the granules morphologies, an accelerating voltage of 10 kV was employed.

### 2.3.3. 3D mapping of dopants in the granules by $\mu$ XRF tomography

The distribution of Fe and Mn dopant atoms in the granules was examined by  $\mu$ -beam scanning X-ray fluorescence ( $\mu$ XRF) contrast tomography. The measurements were performed at the microXAS beamline at the Swiss Light Source synchrotron (Paul Scherrer Institut), using an X-

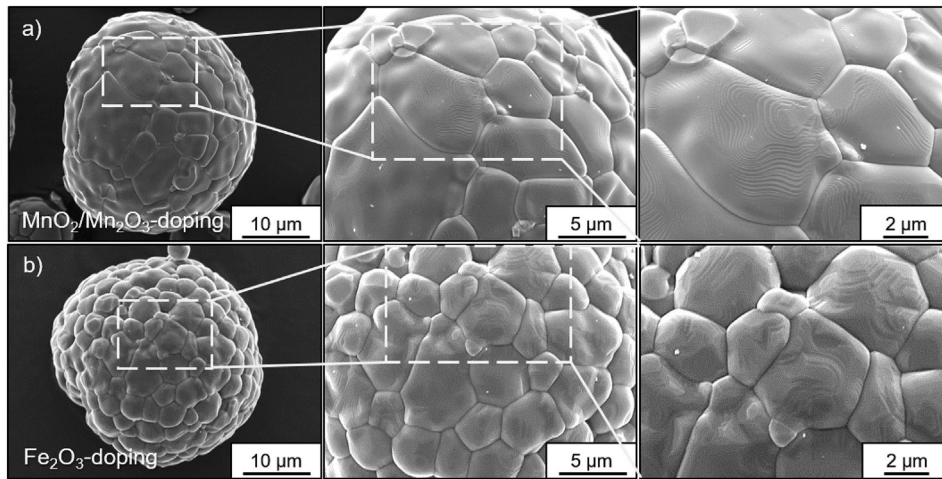


**Fig. 5.** SEM Illustration of grain growth and microstructure evolution in alumina granules after sintering at 1600 °C depending on a)  $\text{MnO}_2/\text{Mn}_2\text{O}_3$  doping or b)  $\text{Fe}_2\text{O}_3$  doping.

ray beam focused down to  $1 \times 1 \mu\text{m}^2$  with an energy of 14.7 keV. Granules were placed in glass capillaries with internal diameter of 100  $\mu\text{m}$ , which were mounted on the rotational stage at the beamline. To visualize the dopant distribution in 3D, the tomography was performed by lateral scanning of the capillary in a continuous manner, at different orientations equally spaced over  $180^\circ$ . The X-ray fluorescence signal was recorded simultaneously along with the incoming and transmitted intensity for every micrometer of the sample, using dwell time of 200 ms. The XRF signal was recorded using two silicon drift detectors, the transmitted intensity with a SiC diode and the incoming one with a mini ionization chamber. This procedure was performed at different positions along the axial direction of the cylindrical capillary, and afterwards the sample was analyzed slice by slice. Each analyzed slice in a volume was separately scanned, reconstructed and afterwards stitched together into a 3D volume. More information about the measurement method can be found in Sanchez et al. [50].

#### 2.3.4. High resolution synchrotron powder diffraction

To identify major and minor crystallographic phases before and after thermal treatment, high resolution powder diffraction measurements were conducted at Material Science (MS) beamline at the Swiss Light Source (PSI) synchrotron [51]. The energy of the beam set for powder diffraction measurements was 12.398 keV and the wavelength was 1.0009 Å, which was evaluated based on the measurement of the SI standard from NIST. As-prepared and thermal treated granules as well as the starting powders were measured in glass capillaries (diameter 200  $\mu\text{m}$ ) in a transmission mode (Debye-Scherrer geometry). Rietveld refinement using TOPAS Bruker AXS software was used to quantify the crystallographic phases.

#### 2.3.5. Powder absorption measurements

The absorption of the powders for laser processing was quantified with an integrating sphere (Gigahertz-Optik UPB-150-ARTA, Gigahertz-Optik GmbH, Germany) equipped with a detector (power meter Ophir 10 A) and coated with barium sulfate in accordance to Florio et al. [16]. The layer thickness of 100  $\mu\text{m}$  and the green pulsed laser (IPG GLPM-5) were selected to recreate similar absorption conditions like in the SLS/SLM process. Temperatures during the measurement were assumed to be close to room temperature, since a laser power of only 1 W and a distance of focus to sample of 160 mm were used. The measurable power range was 15  $\mu\text{W}$  - 3 W. By measuring the reflectivity  $R$  and transmission  $T$  of the sample in two different positions, the absorption  $A$  in % was calculated as:

$$A = 1 - R - T \quad (1)$$

A qualitative absorption measurement of the powders for a wavelength range of 300–1500 nm (in 2 nm steps) was performed with the Shimadzu 3600 UV-VIS-NIR spectrophotometer (Shimadzu Corporation, Japan). Since powder induces complex scattering of light, the Kubelka-Munk method for measurements of diffuse reflectance was chosen. Assuming an infinite thickness of the powder layer (thick enough that a further thickness increase does not change the reflectance), a ratio of arbitrary constants of absorption (absorption coefficient  $K$ ) and scattering (scattering coefficient  $S$ ), can be calculated by measuring the reflectance of the sample [52,53]:

$$\frac{K}{S} = \frac{(1 - R')^2}{2R'} \quad (2)$$

A requirement for the Kubelka-Munk theory is a significant stronger scattering in the medium than absorption and that the scattered radiation is isotropic so that the reflection at the surface is negligible, which is usually the case for bright and dull colors. To achieve these requirements a weight ratio of sample to  $\text{BaSO}_4$  powder (Nacalai Tesque Inc., Japan) of 1:9 was homogeneously mixed and compacted in a sample holder (depth: 6 mm; diameter: 25 mm) before the measurements.  $\text{BaSO}_4$  serves as a reference material, since it offers almost complete scattering of the used monochromatic light. To account for the reflectance and the residual absorption in the  $\text{BaSO}_4$  powder, the quantity  $R'$  was determined as the ratio of the reflectance of the compacted mixed powder  $R_p$  to that of the compacted, pure  $\text{BaSO}_4$  powder  $R_0$  [52,53]:

$$R' = \frac{R_p}{R_0} \quad (3)$$

A qualitative absorption spectrum was finally given by plotting the  $K/S$  ratio over the wavelength. For the doped granules with and without coarse alumina AA18 the corresponding wavelength  $\lambda$  for calculation of the bandgap was evaluated by direct fitting from this absorption spectrum. For a better comparison, both spectra were normalized. The bandgap energy was calculated from the following equation:

$$E_p = \frac{hc}{\lambda} \frac{1}{e} \quad (4)$$

using elementary charge  $e$ , Planck's constant  $h$  and the speed of light  $c$ .

#### 2.4. Laser processing

The laser processing was performed by the Institute of Machine Tools and Manufacturing at ETH Zurich using a green (532 nm) pulsed laser (IPG GLPM-5) with a pulse duration of 1.5 ns, a repetition rate of 300 kHz



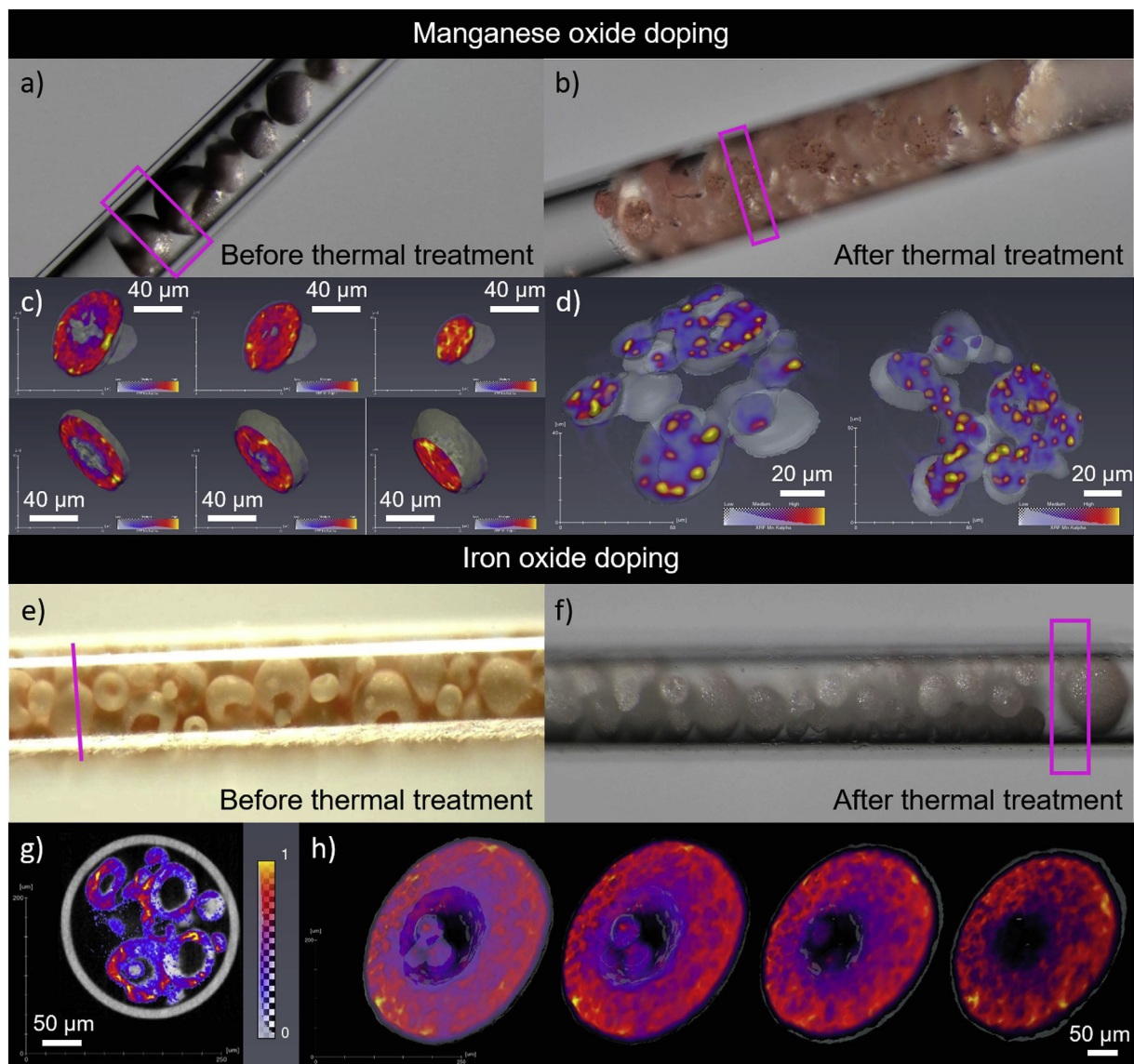


**Fig. 6.** Optical microscopy images and X-ray fluorescence contrast tomography of the Mn- (a–d) and Fe-doped (e–h) granules before (a, c, e, g) and after thermal treatment at 1600 °C (b, d, f, h). The color scale indicates the intensity of X-ray fluorescence of Fe K $\alpha$  (yellow-high, red-medium, blue-low), which is a measure of Fe atoms concentration (lack of Fe atoms is indicated by gray color). (For interpretation of the references to color in this figure legend, the reader is referred to the Web version of this article.)

and a nominal average output power of 5 W. The in-house built experimental SLM machine used for processing was described in detail in Florio et al. [16]. The applied laser parameters were a spot diameter of 135 μm, a hatch distance of 135 μm, a laser power of 5.75 W and a scanning speed of 2 mm/s.

### 2.5. Characterization of SLM and SLS manufactured parts

The SLM printed cubic ceramic parts were representatively imaged by optical microscopy (SterEO Discovery.V20, Carl Zeiss Microscopy, Germany). To visualize the internal structure of the parts, SEM and X-ray tomographic microscopy at the TOMCAT beamline of the Swiss Light Source were performed. Before the analysis of the microstructure by SEM, the samples were cold embedded in a resin (CaldoFix-2, Struers GmbH, Switzerland). Afterwards the cross-sections were ground, polished (with a 1 μm diamond suspension) and coated with gold-palladium. Tomography scans were performed using a standard setup for full field tomography composed of a 100 micron-thick LuAG:Ce scintillator, an optical microscope with 4 $\times$  magnification and a sCMOS camera, which

provides a field of view of 4.2 mm  $\times$  3.5 mm with 1.625 μm pixel size. The used energy of the X-ray beam was 25 keV. 1501 projections were acquired over 180° with 280 ms exposure time per projection. 3D imaging of 3  $\times$  3  $\times$  3 mm<sup>3</sup> sized cubes allowed to visualize and quantify cracks and pores with a spatial resolution of about 3 μm. Accuracy of the density evaluation from tomographic microscopy was determined by obtained contrast and spatial resolution. The error estimated for these measurements was ca. 0.1%. Phase composition after laser printing was evaluated from powder diffraction measurements of crushed samples, as described in section 2.3.4.

## 3. Results and discussion

### 3.1. Homogeneous dispersion of starting materials in water

The absolute densities, the specific surface area (SSA) and the resulting BET average particle size of the raw powders were determined before the dispersing step. The results are summarized in Table 1.

The density measured for Fe<sub>2</sub>O<sub>3</sub> L2715D was in good accordance with

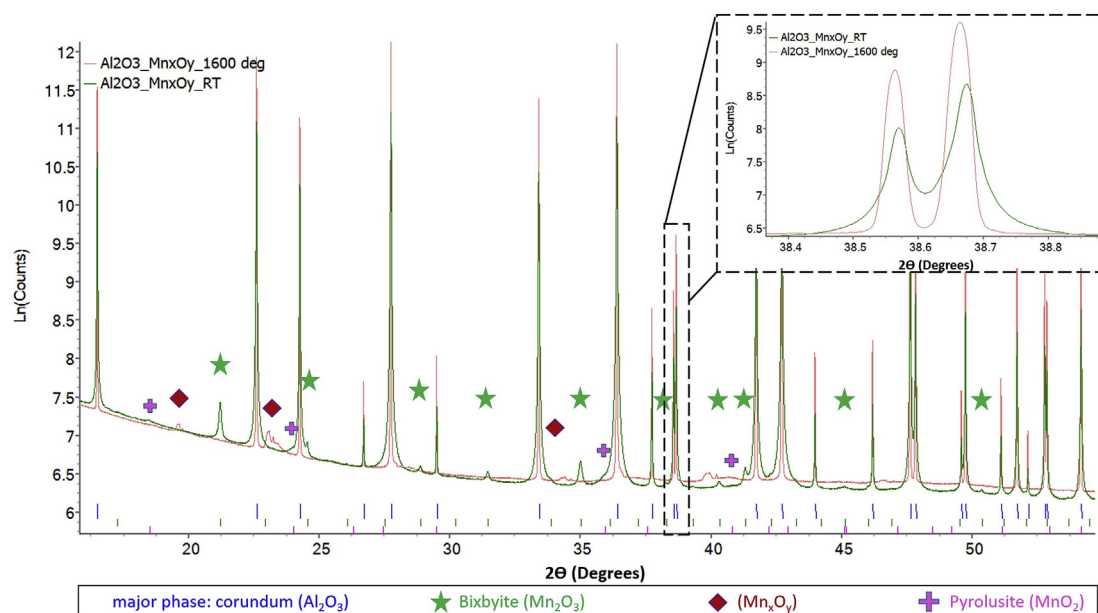


Fig. 7. High resolution powder diffraction of the Mn-doped granules with peak enlargement to illustrate the implementation of Mn ions within corundum lattice.

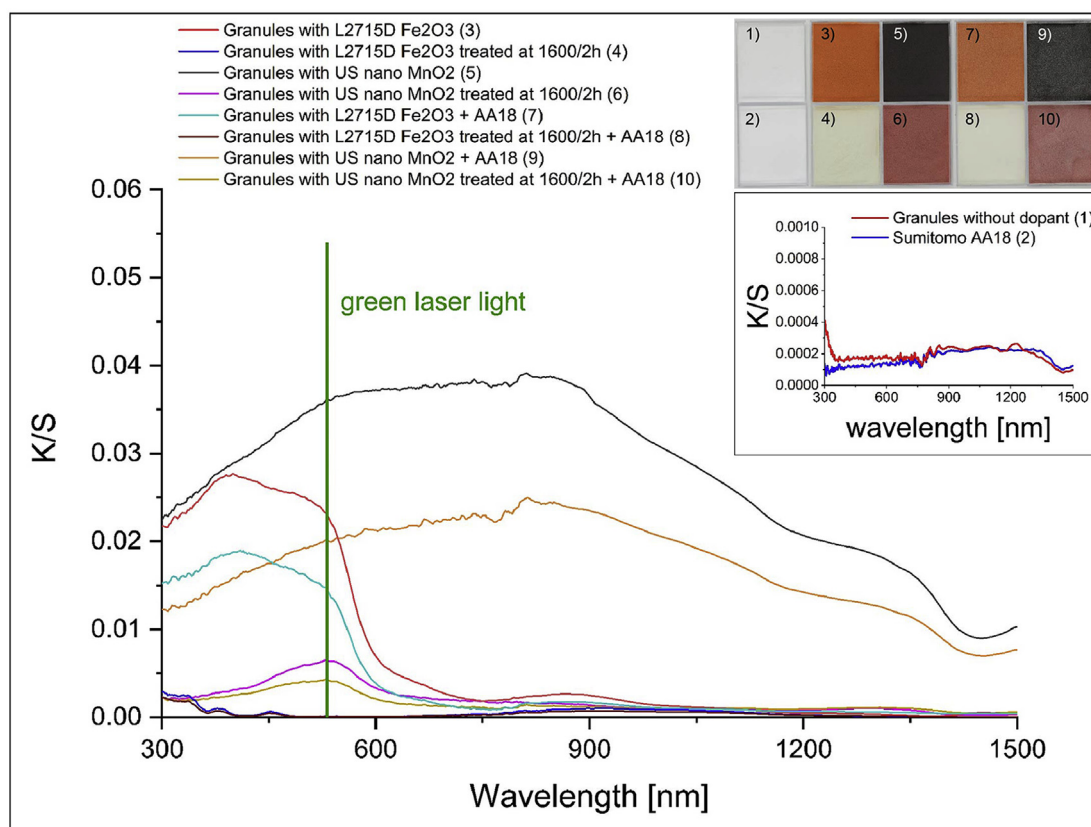


Fig. 8. Qualitative absorption spectrum for spray dried powders evaluated by the Kubelka Munk method for measurements of diffuse reflectance given by plotting K/S ratio over wavelength.

the company given values, whereas the density of the  $\text{MnO}_2$  US3319 of  $4.28 \text{ g/cm}^3$  differs significantly from the company quoted value of  $5.03 \text{ g/cm}^3$ . This can be explained by the powder in nanoscale and a significant amount of  $\text{Mn}_2\text{O}_3$  (68%) with a theoretical density of  $4.5 \text{ g/cm}^3$ , as seen by XRD. By this method, L2715D was identified as 75%  $\alpha\text{-Fe}_2\text{O}_3$  and 25%  $\gamma\text{-Fe}_2\text{O}_3$ . The measured densities for the organic materials were  $1.23 \text{ g/cm}^3$  for PEG35000 and  $1.60 \text{ g/cm}^3$  for ammonium citrate dibasic.

Ammonium citrate dibasic was previously found to be a suitable dispersant for all used alumina powders and  $\text{Fe}_2\text{O}_3$  L2715D [31] (Fig. 1b). By adsorption on the particle surfaces citrate causes an exchange of hydroxyl groups with carboxylate ions and the so created negative surface charge enables a homogeneous dispersion [31,54]. Since the  $\text{MnO}_2/\text{Mn}_2\text{O}_3$  nanoparticles were initially positively charged (39.9 mV) (Fig. 1a), the dispersion by ammonium citrate dibasic was



**Table 3**

Absorptance, reflectance and transmission values of the green laser light in the powder bed measured by an integrating sphere.

Powder	Reflectance [%]	Transmittance [%]	Absorptance [%]
Granules without dopant (1)	82.5	5.9	11.6
Sumitomo AA18 (2)	84.3	6.8	8.9
Granules with Fe <sub>2</sub> O <sub>3</sub> (3)	13.6	0.0	86.4
Granules with Fe <sub>2</sub> O <sub>3</sub> treated at 1600 °C/2 h (4)	79.9	3.8	16.3
Granules with MnO <sub>2</sub> /Mn <sub>2</sub> O <sub>3</sub> (5)	7.5	0.0	92.5
Granules with MnO <sub>2</sub> /Mn <sub>2</sub> O <sub>3</sub> treated at 1600 °C/2 h (6)	14.6	0.0	85.4
Granules with Fe <sub>2</sub> O <sub>3</sub> + AA18 (7)	18.1	0.0	81.9
Granules with Fe <sub>2</sub> O <sub>3</sub> treated at 1600 °C/2 h + AA18 (8)	82.2	5.2	12.6
Granules with MnO <sub>2</sub> /Mn <sub>2</sub> O <sub>3</sub> + AA18 (9)	11.9	0.0	88.1
Granules with MnO <sub>2</sub> /Mn <sub>2</sub> O <sub>3</sub> treated at 1600 °C/2 h + AA18 (10)	22.0	0.0	78.0

**Table 4**

Properties of powders used for laser processing, which contain coarse alumina AA18 and spray dried granules doped with either iron oxide or manganese oxide.

Powder	Final powder 1	Final powder 2	Final powder 3	Final powder 4
Composition	70 vol% Fe <sub>2</sub> O <sub>3</sub> -doped granules +30 vol% coarse alumina AA18	70 vol% MnO <sub>2</sub> /Mn <sub>2</sub> O <sub>3</sub> -doped granules +30 vol% coarse alumina AA18	70 vol% Fe <sub>2</sub> O <sub>3</sub> -doped granules treated at 1600 °C/2 h + 30 vol% coarse alumina AA18	70 vol% MnO <sub>2</sub> /Mn <sub>2</sub> O <sub>3</sub> -doped granules treated at 1600 °C/2 h + 30 vol% coarse alumina AA18
Solid load in slurry [vol %]	49.8	49.6	49.8	49.6
Dopant amount [vol%]	0.6	0.8	0.6	0.8
Apparent density [% of AD]	42.9	44.2	45.1	48.4
Tapped density [% of AD]	50.9	51.9	53.2	56.4
Absolute density [g/cm <sup>3</sup> ]	3.889	3.858	4.022	3.973
Hausner ratio	1.19	1.18	1.18	1.17
Moisture content [wt %]	1.26	0.72	0.12	0.10
d <sub>10</sub> [μm]	17.5	17.4	20.0	18.5
d <sub>50</sub> [μm]	32.1	30.5	43.8	40.5
d <sub>90</sub> [μm]	65.4	58.2	94.6	97.1

expected to be as efficient as for Fe<sub>2</sub>O<sub>3</sub>. The isoelectric point could be easily adjusted at a pH saturation value of 3 like for the Fe<sub>2</sub>O<sub>3</sub> nanoparticles. The evaluated saturation amounts of ammonium citrate dibasic on the nanoparticles surfaces for further dispersion were 1.5 wt% (4.0 vol %) for MnO<sub>2</sub>/Mn<sub>2</sub>O<sub>3</sub> and 3.1 wt% (8.4 vol%) for Fe<sub>2</sub>O<sub>3</sub> (Fig. 1c).

However, homogeneous dispersion of MnO<sub>2</sub>/Mn<sub>2</sub>O<sub>3</sub> nanoparticles in water was not straight forward. By adding the saturation amount of ammonium citrate dibasic (Fig. 1d) a negatively charged surface could be indeed created, though the zeta-potential was only around −15 mV for the starting mixture. A pH-adjustment with NaOH to a pH of 10 delivered

a zeta potential shift to a higher value of −36 mV, but a consecutive acid titration (HCl) gave other zeta potential values than measured during base titration. This could be due to MnO<sub>2</sub>/Mn<sub>2</sub>O<sub>3</sub> dissolution at higher pH values. A steady increase of the conductivity during addition of NaOH and HCl (Fig. 1e) confirms this assumption, since more particles provided more charge. However, in the total volume change to achieve a certain pH value (Fig. 1f) no extreme increase was apparent above a pH of 8, which does not totally confirm the assumption of MnO<sub>2</sub>/Mn<sub>2</sub>O<sub>3</sub> dissolution.

To ensure an adequate dispersion of MnO<sub>2</sub>/Mn<sub>2</sub>O<sub>3</sub> in water with the saturation amount of ammonium citrate dibasic, the pH of the solution was increased by the addition of ammonium hydroxide solution, with regard to the increasing zeta potential. The volume based particle size distributions determined by dynamic light scattering (DLS) and laser diffraction (LD) revealed agglomerates for a pH of 7.6 and a pH of 9.8 (Fig. 2a and b). An explanation for this could be, that for pH values smaller than 8.1 the negative charge of the particle surfaces is too small for a proper electrostatic stabilization of the dispersion. At a pH value of 9.8 the assumption of manganese oxide dissolution made due to the steady growth of the conductivity was affirmed by the measured agglomerates. The volume based DLS measurement as well as the volume based LD measurement showed a very similar distribution for MnO<sub>2</sub>/Mn<sub>2</sub>O<sub>3</sub> nanoparticles dispersed at a pH of 8.1 and a pH of 8.6. The values for d<sub>10</sub>, d<sub>50</sub> and d<sub>90</sub> at these two pH values are listed in Table 2. Although a zeta potential of only ca. −20 mV was present at this pH value the nanoparticles could be properly dispersed. The evaluated d<sub>50</sub> by both particle size measurements were less than three times higher than the BET average particle size of 61.7 nm, which indicated a proper dispersion of the nanoparticles in water. However, the high refractive index (for LD) and the high absorptivity (for DLS) of the dark MnO<sub>2</sub>/Mn<sub>2</sub>O<sub>3</sub> has to be considered in both measurement methods, since it can influence the evaluated particle size distributions significantly in terms of scattering and backscattering of the incident light.

The volume based DLS distribution and volume based LD distribution of all the other powders dispersed in water are illustrated in Fig. 2c and d, respectively. Particle size distributions of submicron and micron-sized alumina as well as Fe<sub>2</sub>O<sub>3</sub> nanoparticles were already measured and presented in Pfeiffer et al. [31]. The results for d<sub>10</sub>, d<sub>50</sub> and d<sub>90</sub> are summarized in Table 2. For the coarse alumina powders AA3 and AA18, the particle size distributions were only evaluated by laser diffraction, since the particle size was at the upper measurement limit of the dynamic light scattering device. The micron-sized alumina powders with a uniform distribution and the nanopowders could be well dispersed by ammonium citrate dibasic with no agglomerates visible by DLS or LD [31]. In the case of alumina Taimicron TM-Dar, the DLS and LD volume based particle size distribution was similar. For the Fe<sub>2</sub>O<sub>3</sub>, the distribution measured by DLS was shifted to smaller values compared to LD measurements, since the size of the dispersed particles is below the resolution limit of the laser diffraction device. The volume based DLS measurement showed that the particles were mainly smaller than 100 nm.

### 3.2. Influence of different temperatures and holding times on packing density and flowability

Granules directly after spray drying are represented in the supplementary information (Figure S1a and b). In the case of manganese oxide a slightly higher dopant concentration of 1.24 wt% (1.16 vol%) compared to 0.99 wt% (0.91 vol%) of iron oxide was added, since the particle sizes after dispersing were bigger and a worse distribution was expected. Spray drying led in both cases to preferably spherical granules, which contributed to a high flowability necessary for the SLM/SLS process [55, 56]. The size values of the granules with the different dopants (d<sub>10</sub> = 21.8 μm, d<sub>50</sub> = 36.7 μm and d<sub>90</sub> = 63.9 μm for Fe<sub>2</sub>O<sub>3</sub> doped granules and d<sub>10</sub> = 22.0 μm, d<sub>50</sub> = 38.6 μm and d<sub>90</sub> = 70.8 μm for MnO<sub>2</sub>/Mn<sub>2</sub>O<sub>3</sub>-doped granules after spray drying) were quite similar. The spherical shape of the granules was most likely a result of the ultrasonic atomizer as discussed

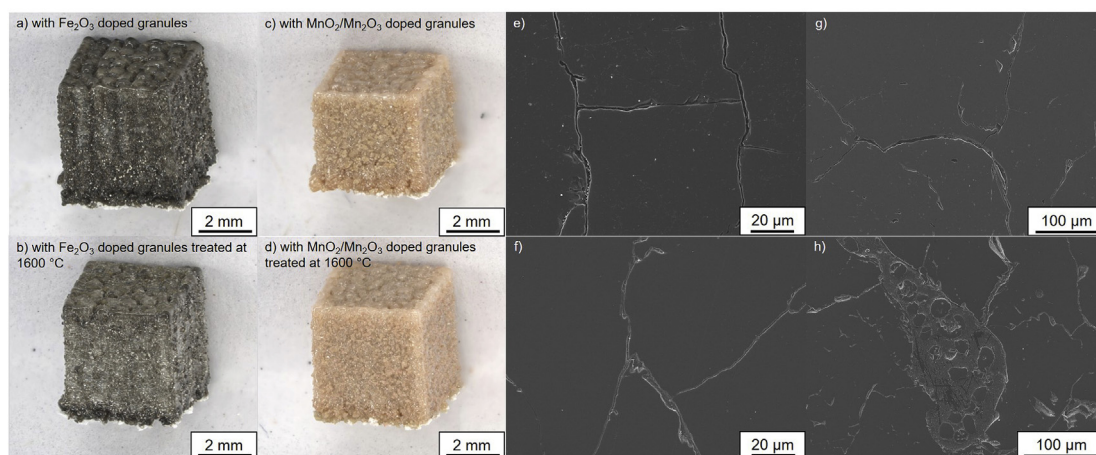


**Fig. 9.** Shape imaged by optical microscopy and internal structure imaged by SEM of laser manufactured parts produced with  $\text{Fe}_2\text{O}_3$ -doped (a, b) and  $\text{MnO}_2/\text{Mn}_2\text{O}_3$ -doped (c, e, g: untreated; d, f, g: pre-treated) powders.

in the authors previous paper [31].

To increase the density,  $\text{Fe}_2\text{O}_3$ -doped  $\text{Al}_2\text{O}_3$  granules were heat-treated in air at temperatures in the range from 1400 up to 1600 °C. As described in the literature the grain growth within the granules was uniform and equiaxed [39] (Fig. 3a–d). At a temperature of 1400 °C the sintering of the alumina was at an early stage, reaching an intermediating stage at 1500 °C and a final sintering at 1600 °C after a holding time of 2 h. Sintering necks between the granules, which formed during thermal treatment (Fig. 3g and h), could be broken by the mixing with coarse alumina AA18 (Fig. 3i). The granules were not destroyed during the mixing process and a homogenous distribution was achieved.

Without the addition of AA18, the apparent density of the granules decreased up to  $-5.0\%$ , since the formed sintering necks worsened the flowability. This could be seen by the increase of the Hausner ratio up to the maximum of 1.394. The tapped density, which was expected to increase after thermal treatment, remained almost unchanged (less than  $0.8\%$  change), since the formed granule agglomerations prevent a close packing of the powder (Fig. 4a). By the aid of AA18 (30 vol% in all mixtures), the apparent and tapped density of the thermal treated powders could be increased by  $+3.6\%$  and  $+6.0\%$ , respectively. Thermal treatment of the granules had only a minor effect on the Hausner ratio in this mixture. Addition of AA18 resulted in significantly better flowability of approximately 1.2 compared to the results without AA18. This could be due to the separation of bonded granules as well as coarse AA18 acting as flowable medium. Further experiments were conducted with a sintering temperature of 1600 °C and a holding time of 2 h, since the difference of the density change was less than  $0.2\%$  and tended towards a minimum (Fig. 4b).

### 3.3. Influence of different dopants on the sintering behavior and effect of thermal treatment on dopant distribution and phase composition

The two different dopants had a different impact on the sintering behavior of the alumina granules. Whereas the iron oxide dopant triggered a uniform and equiaxed grain growth (Fig. 5b), the alumina granules doped with manganese oxide exhibited irregular shaped grains after sintering at 1600 °C (Fig. 5a). Furthermore, the grain growth was more excessive in the case of manganese oxide doping. In both cases the sintering at 1600 °C resulted in dense microstructures with no visible porosity. A promotion of an irregular grain growth by a manganese oxide doping was already described by other groups [33–36]. In contrast to promoting anisotropy and vermicular grain growth in  $\text{Fe}_2\text{O}_3$  doped alumina (up to  $1\%$  reported in Ref. [35] and  $0.8\text{ wt}\%$  reported in Refs. [57]), a uniform and equiaxed grain growth of the granules was observed for a doping of  $1\text{ wt}\%$  and even for  $0.1\text{ wt}\%$ . This could be due to the higher purity of the raw powders, which are available nowadays.

X-ray fluorescence contrast tomography was performed on manganese (Fig. 6a–d) and iron oxide doped (e–h) granules. Manganese oxide doped granules are imaged in Fig. 6a and c before thermal treatment and in Fig. 6b and d after calcination at 1600 °C. Fig. 6e and g correspond to iron oxide doped granules before thermal treatment and Fig. 6f and h to the granules after calcination. The corresponding scanned volumes are illustrated in the optical microscopy images of the capillaries (Fig. 6a, b, f) by the pink rectangles. In case of non-calcinated iron oxide doped granules (Fig. 6e, g), only one slice is presented.

The images in Fig. 6c, d, g and h were obtained by combining volume reconstructed from the  $\mu\text{XRF}$  tomography illustrated by the normalized color scale and obtained from absorption tomography illustrated by the gray scale. Therefore, the color scale corresponds to the distribution of Mn and Fe atoms, respectively, while the transparent gray scale corresponds to the whole material of the granules. Gray color is visible only in volume not occupied by dopant atoms, thus in cases of homogeneous distribution the gray material is hardly visible. These measurements clearly demonstrate the effect of calcination on the distribution of the dopants in the granules, showing that originally well dispersed and homogeneously distributed Mn atoms agglomerate by demixing upon calcination. In contrary, the distribution of Fe atoms becomes even more homogeneous upon calcination at 1600 °C. This observation is in great agreement with the results of the powder diffraction studies presented in Ref. [37], where it was demonstrated that due to calcination at 1600 °C, Fe atoms from hematite nanoparticles are implemented in the corundum lattice and no other phases were formed.

The high resolution powder diffraction of the  $\text{MnO}_2/\text{Mn}_2\text{O}_3$ -doped granules presented in Fig. 7, shows that calcination leads to disappearance of the  $\text{Mn}_2\text{O}_3$  (bixbyite phase), which was the major phase of the manganese oxide dopant particles, and to creation of a very small amount of a different manganese oxide phase. The quantification of this phase from refinement of the powder diffraction data is very challenging, as its amount is in the order of the uncertainty of the technique (below  $0.1\%$ ), therefore it is expected that at least a part of the Mn atoms was implemented in the corundum lattice. This is in agreement with the pink color of the calcined granules. The implementation of Mn ions within corundum lattice is confirmed by the slight change of the lattice constant of corundum (a from  $4.7573\text{ \AA}$  to  $4.7590\text{ \AA}$  and c from  $12.9870\text{ \AA}$  to  $12.9930\text{ \AA}$ ), which was evaluated by the Rietveld refinement and can be seen in the small shift of the corundum peaks (Inlet in Fig. 7).

### 3.4. Absorption and color change of spray dried powders before and after thermal treatment

The qualitative Kubelka Munk spectra revealed a higher absorbance

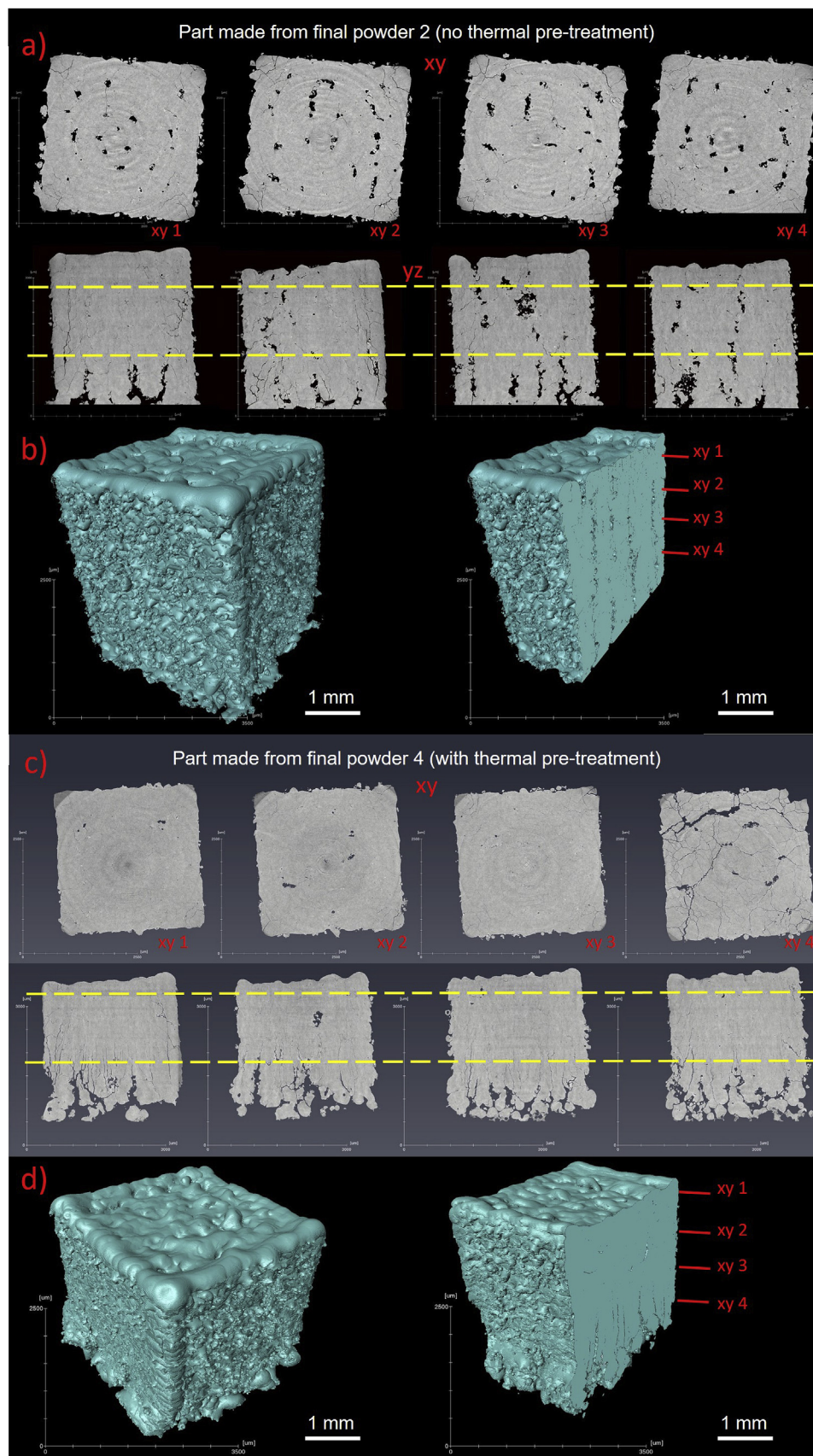


**Fig. 10.** Tomographic microscopy imaging of two parts prepared with a), b) as-prepared (final powder 2) and c), d) heat treated (final powder 4) Mn-doped granules.



over the whole wavelength range from 300 to 1500 nm for blackish  $\text{MnO}_2/\text{Mn}_2\text{O}_3$ -doped granules (powder No. 5 in Fig. 8 and Table 3) than for  $\text{Fe}_2\text{O}_3$ -doped granules (No. 3) (Fig. 8). This could be mainly due to the higher concentration of manganese oxide (0.25 vol%). The manganese oxide doped granules absorbed better at 532 nm (wavelength of used green laser), while the absorption below ca. 400 nm was nearly the same for both dopants. A color change after thermal treatment at 1600 °C was observed for both doped powders. The orange iron oxide doped alumina changed its color to light beige (No. 4). As described in Ref. [37], the  $\text{Fe}^{3+}$  ions diffused first in the nanosized alumina particles at lower temperatures resulting first in two corundum type structures and finally in only one single corundum phase at 1600 °C. Calcination of manganese doped alumina produced magenta colored ceramic granules (No. 6), which was already observed in previous studies [58]. Non-stoichiometric compounds can easily occur during thermal treatment, since manganese cations show a variable valency change and replace the aluminum cations in the lattice [33,34], as already shown for the manganese doped alumina granules by the shift of the alumina peak in Fig. 7. The absorptance decreased for both dopants after thermal treatment. The addition of coarse alumina AA18 led in all cases to a decrease of the K/S ratio (No. 7–10), since pure alumina is a poor absorber in the range of 300–1500 nm, as presented for bimodal alumina granules without dopant (No. 1) and AA18 (No. 2) in the inset on top right side of Fig. 8. The colors of the powders faded after the addition of alumina. Since a clear absorption edge could be only seen for the  $\text{Fe}_2\text{O}_3$  doped granules with and without AA18 (No. 3 and 7), the calculation of the bandgaps was only made for these two samples. The effective bandgap value of the as-prepared granules was 1.98 eV and only slightly smaller than the 2.00 eV for mixed granules indicating a minor effect of the addition of coarse alumina on the bandgap and the optical properties of the powder.

For comparison, the quantitative absorption of the green laser light in the powder bed was measured with an integrating sphere. The measured absorption values for various powders are summarized in Table 3. As for the other measurements,  $\text{MnO}_2/\text{Mn}_2\text{O}_3$  doped alumina granules (No. 5) showed the highest absorption of 92.5% (6.1% higher than for  $\text{Fe}_2\text{O}_3$  doped alumina granules (No. 3)). Thermal treatment of the powders led to lower absorption in both cases (No. 4 and 6). Whereas the absorption of the  $\text{MnO}_2/\text{Mn}_2\text{O}_3$  doped samples dropped only to 85.4%, the absorption of the  $\text{Fe}_2\text{O}_3$  doped alumina granules was only 16.3%, which is only 4.7% more than the value of the pure alumina granules (No. 1) and 7.4% more than measured for coarse AA18 powder (No. 2). In both cases, the thermal treatment initiates a lattice doping of the alumina and additionally, in the case of manganese doping a change of the band structure caused by an oxidation state change, leading to the decreased values in absorbance. By adding the coarse AA18 powder to all granules (No. 7–10), the measured absorptions by the integrating sphere showed the same decreasing effect like in the Kubelka Munk measurements. The values decreased within a range of 3.7–7.4%.

Both techniques gave similar results for all of the tested materials with only two exceptions. The K/S ratio of the as-prepared manganese doped granules mixed with coarse alumina (No. 9) was slightly below the value of iron oxide doped granules (No. 3) at 532 nm in the Kubelka Munk plot, whereas the quantitative measurement showed a higher absorption for the manganese oxide doped sample. Since it is only a small deviation, it could be within the error range of the measurements. Another inconsistency was between thermal treated  $\text{MnO}_2/\text{Mn}_2\text{O}_3$ -doped granules (No. 6) and  $\text{Fe}_2\text{O}_3$ -doped granules mixed with coarse alumina (No. 7), where the values had a bigger difference.

Even if in both measurements the absorption values for the thermal treated  $\text{Fe}_2\text{O}_3$  doped granules were low, both calcined and non-calcined powders could be successfully additively consolidated by the laser. Since the excitation energy of the laser photons is smaller than the bandgap, it could be possibly explained, that granules with homogeneously distributed color centers (Fe-atoms) within the  $\text{Al}_2\text{O}_3$  lattice after thermal treatment [37], can absorb the green laser light at lower temperatures by multiphoton absorption or by excited state absorption, where

the high heat flux of the laser generates a constant intermediate energy level [59]. The absorption measurements in the present work evaluate only the absorptance of the powder bed at room temperature and this does not take into account the dynamics of the whole SLM process. However, it was already shown that optical powder properties at room temperature are also important in order to stabilize the process [16]. With increasing temperature the absorption of alumina can increase. This was already shown for laser excitation [60,61]. In the particular case of doped alumina, a change of the band structure caused by an oxidation state change of the dopant as well as a change of the substrate absorbance during processing has to be considered for absorption at higher temperatures.

### 3.5. Influence of thermal treatment of powders on properties of laser manufactured parts

The properties of the final powders used for laser processing are summarized in Table 4. 30 vol % of AA18 was added to manganese oxide and iron oxide doped granules, firstly following spray drying and secondly after spray drying and subsequent thermal pre-treatment, resulting in four powders in total. The highest apparent (48.4%) and tapped (56.4%) densities were obtained for thermal treated manganese oxide doped granules, which could be due to the larger grain growth as described in section 3.3. All final powders shown a comparable flowability (Hausner ratio between 1.17 and 1.19) for comparable processing conditions with the laser. Thermal treatment resulted in an increase of powder particle size, which can be explained that still bonded granules were present and not totally separated by the added AA18.

In Fig. 9 the geometries and the internal structure of parts manufactured by green pulsed SLM (parameters defined in chapter 2.4.) are representatively illustrated by optical and scanning electron microscopy images. The dimensions of the lateral areas of all parts is accurate. A rough surface is apparent on the lateral and even more on the top areas. The reason for the top surface roughness could be the formation of a melt pool cavity (key hole) by melt pool dynamics induced by evaporation of the material during laser manufacturing and the powder spattering effect, which are proportionally bigger for pulsed lasers compared to a continuous wave laser, or a high viscosity of the melt. Scanning electron microscopy revealed various laser-induced cracks within the microstructure of all samples, which were caused by huge thermal gradients during laser processing. The AA18 alumina phase is totally molten during laser processing in the bulk part of the sample (Fig. 9g). However, coarse AA18 particles can remain together with the spray dried granules in the pores of the sample (Fig. 9h). The black color of the parts processed from iron oxide doped granules, was already explained in Ref. [16] by the formation of hercynite phase ( $\text{FeAl}_2\text{O}_4$ ) during processing. First tests showed hereby that the amount of hercynite in the final part could be diminished by thermal treatment. Understanding of this spinel phase formation is one aspect of the ongoing work. In the case of ceramic parts processed with manganese oxide doped granules, a combination of corundum lattice doping by manganese atoms and the formation of the galaxite phase ( $\text{MnAl}_2\text{O}_4$ ) was found to be the reason for the orange color. A high resolution powder diffraction of the laser manufactured parts with a peak enlargement to illustrate the formed galaxite phase is presented in Figure S2. The volume expansion, caused by the spinel formation from the well-dispersed dopants, can also lead to crack formation during this rapid process. The challenge of thermal stress reduction and thus a diminution of crack formation is still a major issue of the ongoing research.

Fig. 10 presents the results of tomographic microscopy experiments of two parts prepared with manganese oxide doped non-calcined final powder 2 (Fig. 10a and b) and calcined final powder 4 (Fig. 10c and d). Two laser-manufactured samples were imaged for each powder using tomographic microscopy. The reconstructed 3D volumes clearly show the presence of cracks and pores in the samples. Fig. 10 a and c show virtual tomographic slices perpendicular to the build and scanning directions, respectively. By segmentation of the phases (alumina, pores) in the

reconstructed volumes, the density of the parts was evaluated. From the visualization of the structure, it is apparent that the bottom of the samples has a significantly higher amount of cracks and pores. It was observed that the roughness of the top surface and the cracks at the bottom part strongly affect the evaluated density values. Therefore, the density was evaluated for the whole volume and for a region selected inside the samples, where the effects of the substrate and of the top roughness were avoided (the region limited by the dashed yellow lines in Fig. 10 a and c). The density values evaluated for the whole volume were 96.2% for parts from calcined and 94.6% from non-calcined powder. In comparison, the densities evaluated for the selected inner region were 98.6% and 96.2%, respectively. The sample manufactured from pre-treated powder exhibits noticeably higher density, which is very well seen in Fig. 10. This is most likely due to the higher powder bed density of the thermal pre-treated final powder. Furthermore, a porosity arising by trapped CO<sub>2</sub>, which could not easily evaporate during laser processing, could lead to a density decrease in parts from non-calcined final powder 2. Since the residual organic used for spray drying (ca. 4.6 vol% binder and dispersant) within the pre-treated granules was totally burned out during thermal treatment, the influence of CO<sub>2</sub> formation on porosity could be excluded in these samples. The final densities of parts made from pre-treated powder are similar to the density of 97.5%, which Juste et al. [21] measured according to the Archimedes principle for parts manufactured with a continuous wave fibre laser from graphite containing alumina granules. In the present work, a higher density of the powder bed caused a higher density of the final alumina parts, which is in agreement with the literature [17,18]. This confirms the findings in the authors previous work, in which laser processing of iron oxide doped powders with a tapped powder density of 48.4% led to a density of the ceramic sample of 96.1% and a tapped density of 44.3% to a part density of only 93.7% [31]. In comparison to this, Verga et al. [28] reported a density of 96% with a tapped density of 41% for alumina toughened zirconia parts produced with a continuous wave 200 W Nd-YAG fiber laser operating at 1064 nm. The achieved density values were similar, however the used laser and the material were different.

The used porous foam substrate is very helpful as supporting structure to initiate a growing of the laser manufactured ceramic part and for an easy removal after processing. Thermal stresses are reduced by the porous structure in the bottom part. However, the presented 3D visualization of the inner structure shows in both cases a much higher amount of defects in the region close to the porous alumina substrate, which are oriented in the growing direction. Therefore, the bottom part should be removed mechanically after processing.

Cross sections of parts printed from both powders were analyzed by electron microscopy as well as tomographic microscopy and revealed the presence of unmolten granules within the pores (Figure S3), which confirmed that not all granules were affected during laser processing and that the internal structure of the granules changes upon calcination. The detailed description is given in the supplementary information.

#### 4. Conclusions

Ceramic parts with relative densities up to 98.6% were produced by green pulsed laser sintering and melting of doped aluminum oxides granules with a laser power of 5.75 W. Nano manganese oxide was introduced as a convenient dopant (amount of 1.2 vol%) to improve the laser absorption by 80.9% in comparison to undoped alumina granules. The approach taken shows the benefits of customized manganese oxide and iron oxide doped aluminum oxide powders to enable a processing with the desired laser, which was not possible with commercially available undoped powders. Thermal pre-treatment of the granules was shown to affect microstructure, dopant distribution, phase composition and density of the granules and the density of the final parts. The following conclusions can be drawn:

- The dopants had an impact on the sintering behavior of the alumina granules. Iron oxide dopant triggered a uniform, equiaxed grain growth, whereas the manganese oxide resulted in an irregular, more excessive growth of the grains.  $\mu$ -Beam X-ray fluorescence tomography confirmed a uniform distribution of both dopants after spray drying, but also revealed, that originally well-distributed Mn atoms demix upon thermal treatment. High resolution powder diffraction revealed a partial incorporation of Mn-atoms and a total incorporation of Fe-atoms within the corundum lattice.
- Thermal pre-treatment of manganese oxide and iron oxide granules, along with the addition of coarse alumina to break sintering necks, resulted in increased tapped powder densities, which attained values of up to 56.4% of the theoretical density. Consequently, laser sintering of the thermally pre-treatment powders resulted in an increase of the final-part densities. In order to exclude the influence of the flowability on the final density of the processed parts, the Hausner ratio of all powders was fixed between 1.17–1.19.

#### Declaration of competing interest

The authors declare that they have no known competing financial interests or personal relationships that could have appeared to influence the work reported in this paper.

#### Acknowledgements

An exceptional thank goes to the ETH Board for funding the “FUORCLAM” project within the frame of the SFA (Strategic Focus Areas) Advanced Manufacturing. The authors thank Dr. Clark Ligon and Dr. Jon Bell for proofreading the text. We acknowledge the Paul Scherrer Institut, Villigen, Switzerland for provision of synchrotron radiation beamtime at beamlines Tomcat, micro-XAS and MS of the Swiss Light Source and would like to thank Dr. Nicola Casati (PSI) for assistance.

#### Appendix A. Supplementary data

Supplementary data to this article can be found online at <https://doi.org/10.1016/j.oceram.2020.100007>.

#### References

- [1] T. Mühler, C.M. Gomes, J. Heinrich, J. Günster, Slurry-based additive manufacturing of ceramics, *Int. J. Appl. Ceram. Technol.* 12 (1) (2015) 18–25.
- [2] A. Gähler, J.G. Heinrich, J. Günster, Direct laser sintering of Al<sub>2</sub>O<sub>3</sub>-SiO<sub>2</sub> dental ceramic components by layer-wise slurry deposition, *J. Am. Ceram. Soc.* 89 (10) (2006) 3076–3080.
- [3] Y. Wu, J. Du, K.-L. Choy, L.L. Hench, Laser densification of alumina powder beds generated using aerosol assisted spray deposition, *J. Eur. Ceram. Soc.* 27 (16) (2007) 4727–4735.
- [4] J. Deckers, S. Meyers, J.P. Kruth, J. Vleugels, Direct selective laser sintering/melting of high density alumina powder layers at elevated temperatures, *Phys. Procedia* 56 (2014) 117–124.
- [5] H. Exner, P. Regenfuß, R. Ebert, L. Hartwig, A. Streek, S. Klötzer, M. Horn, Lasermikrosintern von keramischen Materialien, *RTEJournal* 3 (3) (2006).
- [6] P. Regenfuß, A. Streek, L. Hartwig, S. Klötzer, T. Brabant, M. Horn, R. Ebert, H. Exner, Principles of laser micro sintering, *Rapid Prototyp. J.* 13 (4) (2007) 204–212.
- [7] Z. Fan, M. Lu, H. Huang, Selective laser melting of alumina: a single track study, *Ceram. Int.* 44 (8) (2018) 9484–9493.
- [8] J. Liu, S. Bai, Femtosecond laser additive manufacturing of YSZ, *Appl. Phys. A* 123 (4) (2017).
- [9] F. Niu, D. Wu, F. Lu, G. Liu, G. Ma, Z. Jia, Microstructure and macro properties of Al<sub>2</sub>O<sub>3</sub> ceramics prepared by laser engineered net shaping, *Ceram. Int.* 44 (12) (2018) 14303–14310.
- [10] Y. Zheng, K. Zhang, T.T. Liu, W.H. Liao, C.D. Zhang, H. Shao, Cracks of alumina ceramics by selective laser melting, *Ceram. Int.* 45 (1) (2019) 175–184.
- [11] Z. Fan, Y. Zhao, Q. Tan, N. Mo, M.-X. Zhang, M. Lu, H. Huang, Nanostructured Al<sub>2</sub>O<sub>3</sub>-YAG-ZrO<sub>2</sub> ternary eutectic components prepared by laser engineered net shaping, *Acta Mater.* 170 (2019) 24–37.
- [12] V.K. Balla, S. Bose, A. Bandyopadhyay, Processing of bulk alumina ceramics using laser engineered net shaping, *Int. J. Appl. Ceram. Technol.* 5 (3) (2008) 234–242.

- [13] S. Bults, J. Vleugels, B. Van Hooreweder, Microwave assisted selective laser melting of technical ceramics, in: Annual international solid freeform fabrication symposium - an additive manufacturing conference, 29, 2018, pp. 2349–2357.
- [14] Y.-C. Hagedorn, J. Wilkes, W. Meiners, K. Wissenbach, R. Poprawe, Net shaped high performance oxide ceramic parts by selective laser melting, *Phys. Procedia* 5 (2010) 587–594.
- [15] J. Wilkes, Y.C. Hagedorn, W. Meiners, K. Wissenbach, Additive manufacturing of ZrO<sub>2</sub>-Al<sub>2</sub>O<sub>3</sub> ceramic components by selective laser melting, *Rapid Prototyp. J.* 19 (1) (2013) 51–57.
- [16] K. Florio, S. Pfeiffer, M. Makowska, N. Casati, F. Verga, T. Graule, H. Van Swygenhoven, K. Wegener, An innovative selective laser melting process for hematite-doped aluminum oxide, *Adv. Eng. Mater.* 21 (6) (2019).
- [17] P. Bertrand, F. Bayle, C. Combe, P. Goeuriot, I. Smurov, Ceramic components manufacturing by selective laser sintering, *Appl. Surf. Sci.* 254 (4) (2007) 989–992.
- [18] B. Qian, Z. Shen, Laser sintering of ceramics, *J. Asian Ceram. Soc.* 1 (4) (2013) 315–321.
- [19] H. Salmang, H. Scholze, *Keramik*, Springer-Verlag Berlin Heidelberg Berlin Heidelberg, 2007.
- [20] K. Flendall, Adhesion: molecules and mechanics, *Science* 263 (5154) (1994) 1720–1725.
- [21] E. Juste, F. Petit, V. Lardot, F. Cambier, Shaping of ceramic parts by selective laser melting of powder bed, *J. Mater. Res.* 29 (17) (2014) 2086–2094.
- [22] M. Mapar, D.Q. Zhang, Z.H. Liu, W.Y. Yeong, C.K. Chua, B.Y. Tay, O. Geramifard, S. Maleksaeedi, F.E. Wiria, Preparation and flowability characterization of ceramic powders for selective laser melting, in: *High Value Manufacturing: Advanced Research in Virtual and Rapid Prototyping*, 2014, pp. 267–271. Leira ,PT.
- [23] M. Mapar, Selective Laser Melting of Ceramic-Based Materials for Dental Applications, Nanyang Technological University, 2014.
- [24] N.K. Tolochko, Y.V. Khlopkov, S.E. Mozzharov, M.B. Ignatiev, T. Laoui, V.I. Titov, Absorptance of powder materials suitable for laser sintering, *Rapid Prototyp. J.* 6 (3) (2000) 155–161.
- [25] L. Ferrage, G. Bertrand, P. Lenormand, Dense yttria-stabilized zirconia obtained by direct selective laser sintering, *Addit. Manuf.* 21 (2018) 472–478.
- [26] S. Chang, L. Li, L. Lu, J.Y.H. Fuh, Selective laser sintering of porous silica enabled by carbon additive, *Materials* 10 (11) (2017).
- [27] L. Moniz, C. Colin, J.-D. Bartout, K. Terki, M.-H. Berger, Laser beam melting of alumina: effect of absorber additions, *JOM (J. Occup. Med.)* 70 (3) (2018) 328–335.
- [28] F. Verga, M. Borlaf, L. Conti, K. Florio, M. Vetterli, T. Graule, M. Schmid, K. Wegener, Laser-based powder bed fusion of alumina toughened zirconia, *Addit. Manuf.* 31 (2020).
- [29] H. Feng, Y. Wang, C. Wang, F. Diao, W. Zhu, P. Mu, L. Yuan, G. Zhou, F. Rosei, Defect-induced enhanced photocatalytic activities of reduced  $\alpha$ -Fe<sub>2</sub>O<sub>3</sub> nanoblades, *Nanotechnology* 27 (29) (2016).
- [30] M. Sharrouf, R. Awad, M. Roumié, S. Marhaba, Structural, optical and room temperature magnetic study of Mn<sub>2</sub>O<sub>3</sub> nanoparticles, *Mater. Sci. Appl.* 6 (10) (2015) 850–859.
- [31] S. Pfeiffer, K. Florio, M. Makowska, D. Ferreira Sanchez, H. Van Swygenhoven, C.G. Aneziris, K. Wegener, T. Graule, Iron oxide doped spray dried aluminum oxide granules for selective laser sintering and melting of ceramic parts, *Adv. Eng. Mater.* 21 (6) (2019).
- [32] X. Zhang, S. Pfeiffer, P. Rutkowski, M. Makowska, D. Kata, J. Yang, T. Graule, Laser cladding of manganese oxide doped aluminum oxide granules on titanium alloy for biomedical applications, *Appl. Surf. Sci.* 520 (2020) 146304.
- [33] H. Erkalfa, Z. Misirli, M. Demirci, C. Toy, T. Baykara, The densification and microstructural development of Al<sub>2</sub>O<sub>3</sub> with manganese oxide addition, *J. Eur. Ceram. Soc.* 15 (2) (1995) 165–171.
- [34] I.B. Cutler, Nucleation and Nuclei Growth in Sintered Alumina, *Kinetics of High Temperature Process Part III*, Technology Press of M. I. T. and John Wiley & Sons 1959, pp. 120–127.
- [35] H.P. Cahoon, C.J. Christensen, Sintering and grain growth of alpha-alumina, *J. Am. Ceram. Soc.* 39 (10) (1956) 337–344.
- [36] M. Sathiyakumar, F.D. Gnanam, Influence of MnO and TiO<sub>2</sub> additives on density, microstructure and mechanical properties of Al<sub>2</sub>O<sub>3</sub>, *Ceram. Int.* 28 (2) (2002) 195–200.
- [37] M. Makowska, S. Pfeiffer, N. Casati, K. Florio, M. Vetterli, K. Wegener, T. Graule, H. van Swygenhoven, Pre-processing of hematite-doped alumina granules for selective laser melting, *Ceram. Int.* 45 (14) (2019) 17014–17022.
- [38] J.J. Rasmussen, G.B. Stringfellow, I.B. Cutler, S.D. Brown, Effect of impurities on the strength of polycrystalline magnesia and alumina, *J. Am. Ceram. Soc.* 48 (3) (1965) 146–150.
- [39] P. Tartaj, J. Tartaj, Preparation, characterization and sintering behavior of spherical iron oxide doped alumina particles, *Acta Mater.* 50 (1) (2002) 5–12.
- [40] R.K. McGeary, Mechanical packing of spherical particles, *J. Am. Ceram. Soc.* 44 (10) (1961) 513–522.
- [41] J. Sauter, Die Grössenbestimmung der im Gemischnebel von Verbrennungskraftmaschinen vorhandenen Brennstoffteilchen: (Mitteilung aus dem Laboratorium für Technische Physik der Technischen Hochschule München), VDI-Verlag 1926.
- [42] K.F. Young, H.P.R. Frederikse, Compilation of the static dielectric constant of inorganic solids, *J. Phys. Chem. Ref. Data* 2 (2) (1973) 313–410.
- [43] M.R. Querry, Optical Constants, Missouri Univ-Kansas City, 1985.
- [44] M.M. Makhlof, Preparation and optical characterization of  $\beta$ -MnO<sub>2</sub> nano thin films for application in heterojunction photodiodes, *Sensor Actuator Phys.* 279 (2018) 145–156.
- [45] G. Yablokova, M. Speirs, J. Van Humbeeck, J.P. Kruth, J. Schrooten, R. Cloots, F. Boschini, G. Lumay, J. Luyten, Rheological behavior of  $\beta$ -Ti and NiTi powders produced by atomization for SLM production of open porous orthopedic implants, *Powder Technol.* 283 (2015) 199–209.
- [46] J.-P. Choi, G.-H. Shin, H.-S. Lee, D.-Y. Yang, S. Yang, C.-W. Lee, M. Brochu, J.-H. Yu, Evaluation of powder layer density for the selective laser melting (SLM) process, *Mater. Trans.* 58 (2) (2017) 294–297.
- [47] J.-P. Choi, G.-H. Shin, S. Yang, D.-Y. Yang, J.-S. Lee, M. Brochu, J.-H. Yu, Densification and microstructural investigation of Inconel 718 parts fabricated by selective laser melting, *Powder Technol.* 310 (2017) 60–66.
- [48] R. Engeli, T. Etter, S. Hövel, K. Wegener, Processability of different IN738LC powder batches by selective laser melting, *J. Mater. Process. Technol.* 229 (2016) 484–491.
- [49] L. Sing Swee, Y. Yeong Wai, E. Wiria Florencia, Y. Tay Bee, Z. Zhao, L. Zhao, Z. Tian, S. Yang, Direct selective laser sintering and melting of ceramics: a review, *Rapid Prototyp. J.* 23 (3) (2017) 611–623.
- [50] D.F. Sanchez, D. Grolimund, M. Hubert, P. Bleuet, J. Laurencin, A 2D and 3D X-ray  $\mu$ -diffraction and  $\mu$ -fluorescence study of a mixed ionic electronic conductor, *Int. J. Hydrogen Energy* 42 (2) (2017) 1203–1211.
- [51] P.R. Willmott, D. Meister, S.J. Leake, M. Lange, A. Bergamaschi, M. Boge, M. Calvi, C. Cancellieri, N. Casati, A. Cervellino, Q. Chen, C. David, U. Flechsig, F. Gozzo, B. Henrich, S. Jaggi-Spielmann, B. Jakob, I. Kalichava, P. Karvinen, J. Krempasky, A. Ludeke, R. Luscher, S. Maag, C. Quitmann, M.L. Reinle-Schmitt, T. Schmidt, B. Schmitt, A. Streun, I. Vartiainen, M. Vitins, X. Wang, R. Wulschleger, The materials science beamline upgrade at the swiss light source, *J. Synchrotron Radiat.* 20 (Pt 5) (2013) 667–682.
- [52] J.M. Olinger, P.R. Griffiths, Quantitative effects of an absorbing matrix on near-infrared diffuse reflectance spectra, *Anal. Chem.* 60 (21) (1988) 2427–2435.
- [53] P. Kubelka, F. Munk, Ein Beitrag zur Optik der Farbanstriche (Contribution to the optic of paint), *Z. Tech. Phys.* 12 (1931) 593–601.
- [54] P.C. Hidber, T.J. Graule, L.J. Gauckler, Citric acid—a dispersant for aqueous alumina suspensions, *J. Am. Ceram. Soc.* 79 (7) (1996) 1857–1867.
- [55] J.S. Reed, Introduction to the Principles of Ceramic Processing, first ed., John Wiley & Sons, Inc., 1988.
- [56] P. Ramavath, M. Swathi, M. Buchi Suresh, R. Johnson, Flow properties of spray dried alumina granules using powder flow analysis technique, *Adv. Powder Technol.* 24 (3) (2013) 667–673.
- [57] J. Tartaj, G.L. Messing, Anisotropic grain growth in  $\alpha$ -Fe<sub>2</sub>O<sub>3</sub>-doped alumina, *J. Eur. Ceram. Soc.* 17 (5) (1997) 719–725.
- [58] S.X. Wang, J. Yang, X.Q. Ouyang, D.H. Han, Synthesis and properties of Mn-doped alumina red pigment prepared by low-temperature combustion-calcination process, *Adv. Mater. Res.* 250–253 (2011) 769–772.
- [59] Y. Deng, Y.L. Du, M.S. Zhang, J.H. Han, Z. Yin, Nonlinear optical properties in SrTiO<sub>3</sub> thin films by pulsed laser deposition, *Solid State Commun.* 135 (4) (2005) 221–225.
- [60] Z. Zhang, M.F. Modest, Temperature-dependent absorptances of ceramics for Nd: YAG and CO<sub>2</sub> laser processing applications, *J. Heat Tran.* 120 (2) (1998) 322–327.
- [61] V.A. Petrov, Abrupt increase of the absorption coefficient of alumina at melting by laser radiation and its decrease at solidification, *Int. J. Thermophys.* 30 (6) (2009) 1938–1959.